

Chiral scatterers designed by Bayesian optimization

Philipp Gutsche^{1,2}, Philipp-Immanuel Schneider³, Sven Burger^{2,3} and Manuel Nieto-Vesperinas⁴

¹Freie Universität Berlin, Mathematics Institute, Arnimallee 6, 14195 Berlin, Germany

²Zuse Institute Berlin, Computational Nano Optics, Takustr. 7, 14195 Berlin, Germany

³JCMwave GmbH, Bolivarallee 22, 14050 Berlin, Germany

⁴Instituto de Ciencia de Materiales de Madrid, Consejo Superior de Investigaciones Científicas, Campus de Cantoblanco, Madrid 28049, Spain

E-mail: gutsche@zib.de

Abstract. The helicity or chirality of scattered light is strongly linked to the dual symmetry of the scatterer. The latter depends on chiral materials or on scatterers which are not superimposable with their mirror image. This inherently yields asymmetric structures of various shapes with many degrees of freedom. In order to explore these high dimensional parameter spaces, numerical simulations and especially optimization strategies are a valuable tool. Here, we optimize the emission of chiral line sources in two-dimensional dimer setups using Bayesian optimization. We deduce relevant objective functions from recent theoretical findings for chiral electromagnetic fields and employ rigorous simulations of Maxwell's equations.

1. Introduction

Several degrees of freedom of light including frequency, amplitude and polarization are controlled and tailored for applications ranging from optical communication to molecular spectroscopy. Recently, more complex light fields such as occurring in spin-orbit interactions [1] have been investigated. Due to its close relation to these phenomena, the helicity of electromagnetic fields is becoming an important quantity in the analysis of nano-optical devices [2].

Furthermore, nano-antennas have been proven a flexible tool for the enhancement of the emission of electromagnetic sources [3]. In order to increase the contrast of signals from handed sources which possess opposing helicities, it has been shown in the framework of dual symmetry [4] that asymmetric scatterers or metamaterials are required in the nano-optical regime where most materials are non-magnetic.

Often, numerical simulations are carried out for obtaining suitable structures. However, due to the required asymmetry, the underlying parameter spaces are mostly high-dimensional and naive optimization strategy fail to provide fast and reliable results. In addition, fabrication requirements of the devices and/or limitations in the illumination techniques need to be taken into account. That is why, sophisticated optimization algorithms are required [5].

Here, we summarize recent descriptions of the helicity and, in its time-harmonic form, the chirality of light: In section 2, we describe the Helicity Optical Theorem and a Chirality Conservation Law. Precedingly, the stochastic Bayesian optimization [6] is briefly described. Finally, in section 4, we will apply both, the theory on helicity and the described optimization strategy, to the control of two-dimensional line sources embedded in magneto-dielectric dimers.

2. Description of optically chiral fields

In standard electrodynamics, dipolar fields are described by the electric \mathbf{p} and magnetic \mathbf{m} dipole moments. The electric and magnetic fields are up to a prefactor of the wave impedance $Z = \sqrt{\mu/\varepsilon}$ dual to one another [7], where ε is the permittivity and μ is the permeability of the medium in which the source is embedded.

Recently, interest in chiral optical fields has been intensified due to the possibility to enhance the near-field response of chiral molecules. By boosting the optical chirality density locally, extinction measurements gain sensitivity [8]. Additionally, the chirality or helicity of light serves as a tool for fundamental understanding of light-matter interactions [4].

Most optical effects can be described by the electric dipole response. In order to observe chiral effects, the quadrupole contribution of the magnetic dipole response needs to be taken into account. Especially, chiral dipoles of well-defined helicity are of interest in this field. Instead of the dipole basis of electric and magnetic dipoles, the chiral dipole basis of positive and negative handedness with $\mathbf{p} = \pm i\mathbf{m}$ has been proven suitable for the description of chiral phenomena [9].

2.1. Helicity Optical Theorem (HOT)

The response of general dipolar sources (\mathbf{p}, \mathbf{m}) to an incident electric and magnetic field $(\mathcal{E}_{\text{inc}}, \mathcal{H}_{\text{inc}})$ is described by the optical theorem:

$$\frac{\omega}{2} \text{Im}(\mathbf{p} \cdot \mathcal{E}_{\text{inc}}^* + \mathbf{m} \cdot \mathcal{B}_{\text{inc}}^*) = \mathcal{W}^{\text{abs}} + \frac{ck^4}{3n} \left(\frac{1}{\varepsilon} |\mathbf{p}|^2 + \mu |\mathbf{m}|^2 \right). \quad (1)$$

The left-hand side describes the extinction of energy, \mathcal{W}^{abs} is the energy absorption and the remaining part is the scattered energy.

In addition to the analysis of energy quantities, a Helicity Optical Theorem has been formulated [2]:

$$\frac{2\pi c}{\mu} \text{Re} \left(-\frac{1}{\varepsilon} \mathbf{p} \cdot \mathcal{B}_{\text{inc}}^* + \mu \mathbf{m} \cdot \mathcal{E}_{\text{inc}}^* \right) = \mathcal{W}_{\mathcal{H}}^{\text{abs}} + \frac{8\pi ck^3}{3\varepsilon} \text{Im}(\mathbf{p} \cdot \mathbf{m}^*). \quad (2)$$

Here, $\mathcal{W}_{\mathcal{H}}^{\text{abs}}$ is the absorption of helicity (or the conversion of chirality as explained in the next section). The left-hand side is the extinction of chirality and it is obvious that the scattered chirality $\text{Im}(\mathbf{p} \cdot \mathbf{m}^*)$ is only non-zero if the electric and magnetic dipole moments are phase-shifted. The chiral dipoles of well-defined helicity mentioned above scatter the magnitude of $\pm |\mathbf{p}|^2$ chirality.

This formalism is well suited for the study of extinction experiments with secondary dipolar sources. In the following, we show an equivalent description in the time-harmonic context: the general chirality conservation law. Proceedingly, we apply this law to the analysis of a primary dipolar source.

2.2. Chirality Conservation Law (CCL)

The interest in the quantity of optical chirality is manifested in its ability to be described by a general conservation law. This conservation can be formulated for arbitrary, including bi-anisotropic, media. The most general form for monochromatic fields read as [10]

$$2i\omega(\mathfrak{X}_e - \mathfrak{X}_m) + \nabla \cdot \mathfrak{S} = \frac{1}{4} \{ \mathcal{J}^* \cdot (\nabla \times \mathcal{E}) + (\nabla \times \mathcal{J}^*) \cdot \mathcal{E} \}. \quad (3)$$

Similarly to the electromagnetic energy, the chirality density is split into an electric $\mathfrak{X}_e = 1/8 \{ \mathcal{D}^* \cdot (\nabla \times \mathcal{E}) + \mathcal{E} \cdot (\nabla \times \mathcal{D}) \}$ and magnetic part $\mathfrak{X}_m = 1/8 \{ \mathcal{H}^* \cdot (\nabla \times \mathcal{B}) + \mathcal{B} \cdot (\nabla \times \mathcal{H}) \}$.

The flux density of optical chirality is $\mathfrak{S} = 1/4 \{ \mathcal{E} \times (\nabla \times \mathcal{H}) - \mathcal{H}^* \times (\nabla \times \mathcal{E}) \}$. The source term on the right-hand side of this continuity equation is of special interest for this study.

Using the current densities \mathcal{J} for electric and magnetic dipoles, (3) yields the HOT in the context of extinction measurements. For the analysis of primary sources, analogous to the case of energy, the conservation of chirality describes the emission X_{emi} , conversion X_{conv} and the far-field accessible chirality flux X_{far} . These quantities are employed for the optimization of chiral effects in the preceding study and are for localized sources derived as:

$$X_{\text{emi}} = X_0 + \frac{1}{2}\omega \int \text{Im}(\mathcal{J}^* \cdot \mathcal{B}_{\text{sca}}) d^3r \quad (4)$$

$$X_{\text{conv}} = -2\omega \int \text{Im}(\mathfrak{X}_e - \mathfrak{X}_m) d^3r \quad (5)$$

$$X_{\text{far}} = \int_{S^2(r \rightarrow \infty)} \text{Re}(\mathfrak{S}) d^2r = X_{\text{emi}} - X_{\text{conv}}. \quad (6)$$

The chirality emission X_{emi} consists of the bulk chirality emission X_0 , which is the chirality emitted from the dipole in absence of any interacting environment, e.g. $X_0 = 0$ for achiral sources. In addition, a term occurs in X_{emi} which depends on the current density \mathcal{J} , i.e. in our case the dipole moments, and the magnetic field \mathcal{B}_{sca} scattered by the object. The integration of the chirality flux in the far-field, $r \rightarrow \infty$, yields the far-field accessible quantity X_{far} . The chirality conversion X_{conv} consists of a bulk and an interface term for piecewise-constant materials [10].

3. Bayesian optimization

Local optimization is a fairly simple task with various well-established methods such as gradient descent or Newton algorithms. However, in complex systems several optima might arise and mostly only the global optimum is of interest. Bayesian optimization with Gaussian processes tackles this problem and is applied in many fields such as robotics, experimental design and environment monitoring.

Recently, it has also been applied to nano-optical devices [5]. Based on this study, we summarize the basic formalism underlying Bayesian optimization and give details on our implementation in the following.

3.1. Basic formalism

The aim of an optimization is to minimize an objective function f depending on the parameters given by \mathbf{x} :

$$\tilde{\mathbf{x}} = \underset{\mathbf{x} \in \mathcal{X}}{\text{argmin}} f(\mathbf{x}), \quad (7)$$

where $\tilde{\mathbf{x}}$ are the parameters of the global minimum of f in the d -dimensional design space $\mathcal{X} \subset \mathbb{R}^d$. The design space might be a d -dimensional hypercube or a general constraint parameter space.

In each search step Bayesian optimization (BO) takes all previously obtained evaluations of f into account to determine promising parameters and is thus able to reach the global minimum with relatively few iterations. BO is based on a statistical model. Due to their flexibility and tractability, Gaussian processes have been proven to be a suitable basis for this model. Here, every evaluation is associated with a normally distributed random variable.

A Gaussian process is defined by a mean function $\mu : \mathcal{X} \rightarrow \mathbb{R}$ and a kernel function $k : \mathcal{X} \times \mathcal{X} \rightarrow \mathbb{R}$ which is positive definite and describes the covariance of the process. The probability of the multivariate Gaussian random variable $\mathbf{Y} = [f(\mathbf{x}_1), \dots, f(\mathbf{x}_N)]^T$ is given by

$$P(\mathbf{Y}) = \frac{1}{(2\pi)^{N/2} |\Sigma|^{1/2}} \exp \left[-\frac{1}{2} (\mathbf{Y} - \boldsymbol{\mu})^T \Sigma^{-1} (\mathbf{Y} - \boldsymbol{\mu}) \right], \quad (8)$$

where $\boldsymbol{\mu} = [\mu(\mathbf{x}_1), \dots, \mu(\mathbf{x}_N)]^T$ are the mean values and $\boldsymbol{\Sigma} = [k(\mathbf{x}_i, \mathbf{x}_j)]_{i,j}$ is the covariance matrix.

Based on already known values of the objective function, it is possible to make statistical predictions about not yet evaluated points in the parameter space by Gaussian process regression. The determination of the next evaluation point is based on the predicted Gaussian distribution of the function value (mean and standard deviation). This information is used in the determination of the next evaluation point \mathbf{x}_{N+1} by an acquisition function $\alpha : \mathcal{X} \times \mathbb{R} \rightarrow \mathbb{R}$:

$$\mathbf{x}_{N+1} = \operatorname{argmax}_{\mathbf{x} \in \mathcal{X}} \alpha(\mathbf{x}, y_{\min}), \quad (9)$$

where $y_{\min} = \min(f(\mathbf{x}_1), \dots, f(\mathbf{x}_N))$ is the currently obtained global minimum.

3.2. Implementation details

Our implementation of BO is based on the Matern-5/2 kernel

$$k(\mathbf{x}, \mathbf{x}') = \sigma^2 \left(1 + \sqrt{5r^2(\mathbf{x}, \mathbf{x}') + \frac{5}{3}} r^2(\mathbf{x}, \mathbf{x}') \right) \exp \left(-\sqrt{5r^2(\mathbf{x}, \mathbf{x}') + \frac{5}{3}} \right) \quad (10)$$

$$\text{with } r^2 = \sum_{i=1}^d (x_i - x'_i)^2 / l_d^2,$$

where σ is the standard deviation and l_1, \dots, l_d describe the length scales of the parameters. As noted in [5] this kernel leads to slightly faster optimizations than the frequently used squared exponential kernel.

The hyper-parameters of the Gaussian process $\omega = (\sigma, l_1, \dots, l_d)$ are unknown. Since they are at the core of the BO optimization strategy, they should be chosen in an optimal fashion. This optimization is a computationally very expensive part of BO. The employed strategy to reduce the computational overhead of the hyper-parameter optimization is presented in [11].

For the acquisition function α , we use the expected improvement

$$\alpha(\mathbf{x}, y_{\min}) = \mathbb{E}[\max_{\mathbf{x}}(0, y_{\min} - f(\mathbf{x}))], \quad (11)$$

where $f(\mathbf{x})$ is the statistical prediction (Gaussian distribution) of the unknown objective function at the position \mathbf{x} . That is, we take the next sample at the point in the parameter space where the expectation value of the one-sided difference $\max_{\mathbf{x}}(0, y_{\min} - f(\mathbf{x}))$ between the currently known minimum y_{\min} and the Gaussian distribution of $f(\mathbf{x})$ is maximized.

The BO employed in this study is implemented in *python*. The Gaussian processes are based on the module *gptools*. Further details may be found in [5] and [11].

4. Automatic design of optically chiral dimers for line sources

In this study, we present the application of BO to a magneto-dielectric dimer showing optically chiral behaviour. Different aims and accordingly different objective functions are employed for the optimization of dual symmetry, i.e. conservation of helicity, as well as the selective emission enhancement for one handedness of dipolar chiral sources. Finally, a scatterer is designed preserving one handedness and changing the opposite handed source into an achiral field in the far-field.

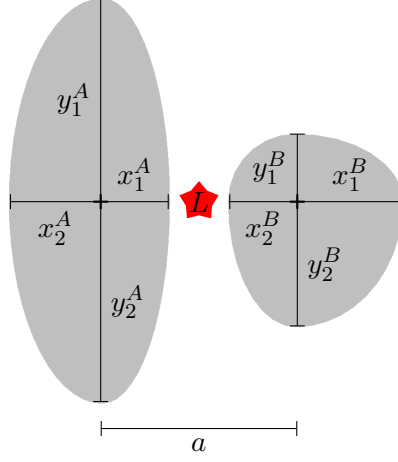


Figure 1. Parametrization of dimer consisting of constituents A and B each with four different radii x_1, y_1, x_2 and y_2 and separated by distance a . Line Source L is placed in the center of the dimer.

4.1. Setup and parametrization

The scatterer analyzed in the following is a dimer consisting of constituents A and B (Fig. 1). The centre points of A and B are separated by the distance a . Each constituent is parametrized by four radii, respectively. This results in a shape given by $(x_i \cos \beta, y_j \sin \beta)^T \subset \mathbb{R}^2$, where x_i and y_j are chosen according to the quadrant and β is the corresponding angle. For example, in the second quadrant: $i = 2, j = 1, \beta \in [\pi/2, \pi]$.

The material of the dimer has a high refractive index of $n = 4$. Accordingly, magnetodielectric effects with high magnetic resonances can be observed, although the material is purely electric with relative permittivity $\epsilon_r = n^2$ and relative permeability $\mu_r = 1$ [12]. This is crucial for the observation of optically chiral behaviour, since for this application spectrally matched electric and magnetic resonances of similar strength are required.

In the centre of the dimer, we place a line source emitting at wavelength λ . Chiral line sources with $\mathbf{p} = \pm i\mathbf{m}$ are analyzed. In order to observe chiral effects despite the underlying z -invariance of the setup, we use $\mathbf{p} \propto (0, 1, 1)^T$. The standard Purcell factor of this two-dimensional source differs only in its prefactor from the well-known formula for a three-dimensional dipole [13]:

$$F_P = 1 + \frac{1}{2W_0} \left\{ \frac{1}{\omega\mu} \text{Im}(\mathbf{p}^* \cdot \mathcal{E}_{\text{sca}}) + k \text{Im}(\mathbf{m}^* \cdot \mathcal{H}_{\text{sca}}) \right\}, \quad (12)$$

where W_0 is the energy radiated by the dipole alone, in absence of any interacting environment. The corresponding chirality emission in (4) for a magnetic and electric dipolar sources is [2]

$$X_{\text{emi}} = X_0 + \text{Re}(\mathbf{p}^* \cdot \mathcal{H}_{\text{sca}}) - \frac{1}{Z} \text{Re}(\mathbf{m}^* \cdot \mathcal{E}_{\text{sca}}). \quad (13)$$

The electromagnetic response of the devices are computed from rigorous solutions of Maxwell's equations. These are obtained with the Finite Element Method implemented in the commercial Maxwell solver *JCMsuite* [14].

4.2. Optimization of dual elliptical dimers

In order to present the optimization procedure in a low-dimensional space, we fix the emission wavelength $\lambda = 950\text{nm}$ and the distance $a = 200\text{nm}$. Furthermore, we set $x_1 = x_2$ and $y_1 = y_2$

for both constituents A and B of the dimer. In addition, the dimer is mirror symmetric, i.e. $x_A = x_B$ and $y_A = y_B$. This leaves two free parameters, x and y for the optimization. Accordingly, A and B are ellipses and it has been shown that ellipsoids are suitable for matching electric and magnetic resonances [15].

The objective function is chosen as the far-field helicity

$$h = \frac{X_{\text{far}}}{kW_{\text{far}}}, \quad (14)$$

where X_{far} is the chirality and W_{far} is the energy measured in the far-field, respectively. The absolute value of $|h| \leq 1$ is limited to unity. Using a negative chiral source, the helicity $h = -1$ describes so-called *dual* behaviour [9] of the dimer: The chirality observed in the far-field is well-defined and has the same value as the chirality of the emitter.

We use BO to minimize h with respect to the ellipse radii $x \in [20, 80]\text{nm}$ and $y \in [20, 210]\text{nm}$. For 16 parallel evaluations of the objective function, the BO requires 122 evaluations in total to obtain a global minimum of approximately -0.956 . This means that only less than 4.4% of the emitted chirality is not preserved. The optimal parameters are $x \approx 68.66\text{nm}$ and $y \approx 150.64\text{nm}$.

As shown in Fig. 2, many different values of h are obtained in the optimization process. The acquired parameters points and their respective objective values are depicted by circles. In addition, Gaussian regression allows for predicting h in the full parameter space and this is shown by the colormap.

In this low dimensional space it is possible for reasonable computational costs to scan the full parameter space which is shown in Fig. 3. In the chosen domain there is only one minimum prominent alongside a larger minimum at the lower corner of the domain. The prediction from BO is very accurate, especially in the surrounding of the global minimum.

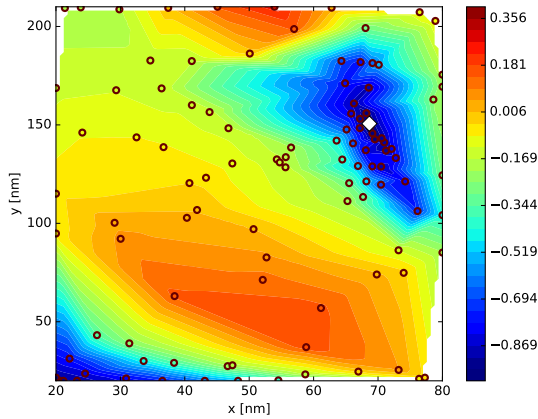


Figure 2. Parameters obtained by BO. Colormap shows Gaussian regression.

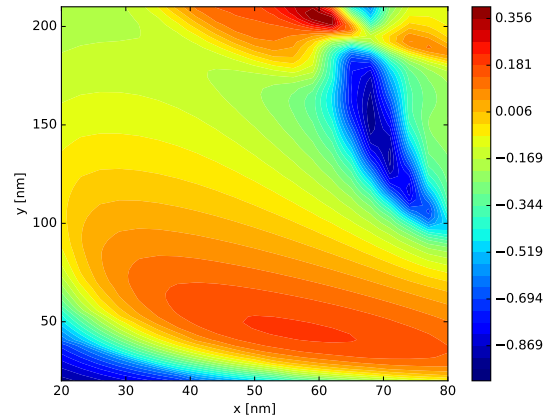


Figure 3. Full parameter space. Colormap shows the objective function.

4.3. Optimization of optically chiral dimers

In the following, we allow optimization of all eight radii and the dimer distance (Fig. 1) resulting in nine free parameters for the BO. Again, we fix the emission wavelength $\lambda = 950\text{nm}$. Assuming non-dispersive media, varying the frequency of the emitter requires only scaling of all geometrical parameters of the optimized structure.

The x -parameter space is limited to $[20, 80]\text{nm}$ and the y parameter space is restricted to $[20, 210]\text{nm}$. The distance a is limited to $[40, 350]\text{nm}$. Furthermore, the following constraint in

the parameter space is employed in order to ensure a minimal distance of the source and the scatterer: $\max(x_1^A, x_2^B) + 20nm - 0.5a < 0$.

For non-mirror-symmetric dimers, it is possible to observe optically chiral effects in the sense that emission of positive and negative chiral sources differ. According to the experimental setup, different quantities might be of interest for the optimization. Here, we optimize for four different objective functions:

- the relative difference of Purcell factors of positive and negative chiral sources

$$f_{g_P}(\mathbf{x}) = g_P = 2 \frac{F_P^+ - F_P^-}{F_P^+ + F_P^-}, \quad f_{g_P} \in [-2, 2] \quad (15)$$

- the relative difference of Purcell factors ensuring a large F_P^-

$$\tilde{f}_{g_P}(\mathbf{x}) = \left\{ \frac{1}{4}g_P + \frac{1}{2} \right\} + \frac{1}{F_P^- + 1}, \quad \tilde{f}_{g_P} \in (0, 2) \quad (16)$$

- the relative difference of scattered helicity in the far-field

$$f_{g_{\text{far}}}(\mathbf{x}) = g_{\text{far}} = |h^+| - |h^-|, \quad f_{g_{\text{far}}} \in [-1, 1] \quad (17)$$

- the relative difference of scattered helicity ensuring a large F_P^-

$$\tilde{f}_{g_{\text{far}}}(\mathbf{x}) = \left\{ \frac{1}{2}g_{\text{far}} + 0.5 \right\} + \frac{1}{F_P^- + 1}, \quad \tilde{f}_{g_{\text{far}}} \in (0, 2) \quad (18)$$

Fig. 4 shows the result of the optimization of all nine parameters for the relative difference of Purcell factors f_{g_P} . The sensitivity of the objective value with respect to the three most sensitive parameters a , y_2^B and x_2^B is given. On the x -axis the variation of the parameters in nm and on the y -axis the predicted change of the objective function is shown. These predictions are derived from Gaussian regression and their standard deviation is depicted with dashed lines.

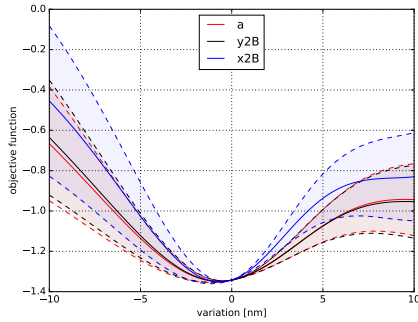


Figure 4. Optimization of f_{g_P} . Most sensitive parameters.

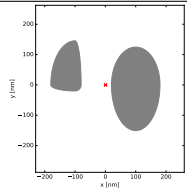
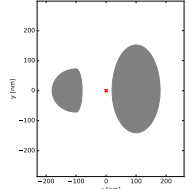
obj. fct.	F_P^-	F_P^+	g_P	opt. geom.
f_{g_P}	8.38	1.65	-1.34	
\tilde{f}_{g_P}	9.56	2.09	-1.28	

Figure 5. Optimization of f_{g_P} and \tilde{f}_{g_P} . Purcell factors, their relative difference and optimal geometries.

The limits in the parameter space are analogous to the optimization of the dual dimer in the previous section. The detailed geometric parameters are given in Tab. A1. Five out of nine parameters are at the upper or lower limit of the parameter hypercube. A larger parameter space might therefore be beneficial for further optimization, however, larger violation of the dual symmetry is expected.

A minimal g_P -factor of -1.34 is achieved by a highly achiral scatterer. Since the emission of negative chiral sources is larger for a negative g_P -factor, the constituent B is as close as possible in the limited parameter space to the source which emits mostly to the right. However, a minimized g_P could also be achieved by purely reducing F_P^+ . That is why, we change to the objective function to \tilde{f}_{g_P} which ensures a large F_P^- .

As shown in Fig. 5, the adjusted objective functions results in an increase of more than 10% in the Purcell factor of the negative chiral source F_P^- . On the other hand, g_P is only decreased by less than 5%. These changes in the objective values are rather small. However, it shows that the objective function has to be chosen carefully to obtain the desired behaviour of the device. This will be more important in the next example.

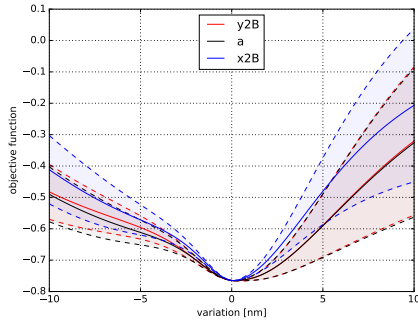


Figure 6. Optimization of $f_{g_{\text{far}}}$. Most sensitive parameters.

obj. fct.	h^+	F_P^-	F_P^+	g_{far}	opt. geom.
$f_{g_{\text{far}}}$	5.3e-6	1.45	0.88	-0.77	
$\tilde{f}_{g_{\text{far}}}$	-5.5e-3	3.57	1.66	-0.68	

Figure 7. Optimization of $f_{g_{\text{far}}}$ and $\tilde{f}_{g_{\text{far}}}$. Far-field chiralities, their rel. difference and optimal geometries.

In addition to the standard Purcell factors, it provides new insight to analyze the helicity or chirality of light. Namely, the far-field helicity (14) is of interest in the analysis of e.g. chiral molecules. Note that the investigated structure is lossless and accordingly $W_{\text{far}} = W_{\text{emi}}$, i.e. the Purcell factor F_P is experimentally accessible in the far-field.

Minimizing the objective function $f_{g_{\text{far}}}$ yields a structure which preserves helicity for negative chiral sources and yields achiral emission in the far-field for positive chiral sources. This could be of interest in order to distinguish both handedness with high accuracy. Detailed geometric parameters of the optimal geometry are given in Tab. A2.

As shown in Fig. 6 and Fig. 7, the BO gives an optimal geometry which basically turns the chiral emission of a positive chiral source into achiral fields in the far-field: the helicity is below 1%. On the other hand, chirality of negative chiral sources is dominantly preserved and less

than 23% of positive chirality is observed in the far-field. Accordingly, g_{far} of the optimized geometry is well suited to distinguish positive from negative chiral sources by analyzing the chirality observable in the far-field.

However, this comes with the disadvantage of relatively low emission enhancement of $F_P^- = 1.45$. Consequently, we change the objective function from optimizing purely g_{far} to $\tilde{f}_{g_{\text{far}}}$ which takes an increase in the Purcell factor into account. Fig. 7 shows that the optimal device is very different from the previous result. Instead of minimizing chirality conversion by decreasing the area of the dimer constituent B to a minimum, the two parts of the dimer are of equal size but different shape.

This approach increases the Purcell factor of the negative chiral source by a factor of nearly 2.5. Nevertheless, g_{far} is decreased to -0.68, still yielding basically achiral far-field behaviour for a positive chiral source but showing higher chirality conversion for negative chiral sources. Since the ratio of F_P^- and F_P^+ is higher for the second optimization, we expect this device having better experimental performance.

In summary, we have shown for standard energy quantities such as the difference of Purcell factors of chiral sources as well as for novel quantities such as the helicity of light that the objective function of the optimization has to be chosen carefully. In the best case, a single objective function is able to take several design goals such as high distinction of positive and negative chiral sources as well as high emission enhancement into account. The choice of different objective function results in geometrically much different devices.

5. Conclusion

We used Bayesian Optimization to optimize the design of two-dimensional dimer structures. Quantities of interest were derived from a general theory of the helicity or chirality of light, namely, the recently introduced Helicity Optical Theorem and Chirality Conservation Law. Even in high-dimensional parameter spaces with nine free parameters, BO is a computationally feasible approach to minimize the number of objective function evaluations and obtain the global minimum in a given parameter space.

We expect that this numerical technique together with the rigorous physical description of optically chiral phenomena, provides further insight into devices for the analysis of chiral phenomena and could give guidelines for experimental realization of measurements of the chirality of light.

Acknowledgments

We acknowledge support by Freie Universität Berlin through the Dahlem Research School and by MINECO-FEDER, grants FIS2012-36113-C03-03, FIS2014-55563-REDC, and FIS2015-69295-C3-1-P.

References

- [1] Bliokh K Y, Bekshaev A Y and Nori F 2017 *Physical Review Letters* **119** 073901
- [2] Nieto-Vesperinas M 2017 *Phil. Trans. R. Soc. A* **375** 20160314
- [3] Abass A, Gutsche P, Maes B, Rockstuhl C and Martins E R 2016 *Optics express* **24** 19638–19650
- [4] Fernandez-Corbaton I 2014 *Helicity and duality symmetry in light matter interactions: Theory and applications* Ph.D. thesis Macquarie University, Department of Physics and Astronomy
- [5] Schneider P I, Santiago X G, Rockstuhl C and Burger S 2017 *Proc. SPIE 10335* p 103350O
- [6] Shahriari B, Swersky K, Wang Z, Adams R P and de Freitas N 2016 *Proc. IEEE* **104** 148–175
- [7] Jackson J D 1998 *Classical Electrodynamics* 3rd ed (John Wiley and Sons)
- [8] Tang Y and Cohen A E 2010 *Physical review letters* **104** 163901
- [9] Zambrana-Puyalto X and Bonod N 2016 *Nanoscale* **8** 10441–10452
- [10] Gutsche P, Poulikakos L V, Hammerschmidt M, Burger S and Schmidt F 2016 *Proc. SPIE 9756* p 97560X
- [11] Garcia-Santiago X, Schneider P I, Rockstuhl C and Burger S 2017 *in preparation*
- [12] Krasnok A, Glybovski S, Petrov M, Makarov S, Savelev R, Belov P, Simovski C and Kivshar Y 2016 *Applied Physics Letters* **108** 211105
- [13] Novotny L and Hecht B 2006 *Principles of nano-optics* (Cambridge University Press)
- [14] Pomplun J, Burger S, Zschiedrich L and Schmidt F 2007 *physica status solidi (b)* **244** 3419–3434
- [15] Lukyanchuk B S, Voshchinnikov N V, Paniagua-Domínguez R and Kuznetsov A I 2015 *ACS Photonics* **2** 993–999

Appendix A. Geometric Parameters

The optimized parameters with f_{g_P} (15) and \tilde{f}_{g_P} (16) as objective functions are given in Tab. A1. Those with objective functions $f_{g_{far}}$ (17) and $\tilde{f}_{g_{far}}$ (18) are given in Tab. A2.

obj. fct.	x_1^A	y_1^A	x_2^A	y_2^A	x_1^B	y_1^B	x_2^B	y_2^B	a
f_{g_P}	20.00	145.51	80.00	20.00	80.00	124.85	80.00	150.51	200.00
\tilde{f}_{g_P}	20.00	72.62	80.00	71.30	79.99	152.40	80.00	140.15	200.08

Table A1. Optimized geometric parameters (Fig. 1) for optimization of relative difference of Purcell factors (15) and (16).

obj. fct.	x_1^A	y_1^A	x_2^A	y_2^A	x_1^B	y_1^B	x_2^B	y_2^B	a
$f_{g_{far}}$	20.00	170.00	32.51	150.31	25.62	21.57	20.19	20.00	291.43
$\tilde{f}_{g_{far}}$	35.42	186.48	62.75	123.69	56.07	176.39	77.99	159.05	196.44

Table A2. Optimized geometric parameters (Fig. 1) for optimization of relative difference of scattered chirality (17) and (18).